Significant Supersonic Modes and the Wall Temperature Effect in Hypersonic Boundary Layers

Carleton P. Knisely* and Xiaolin Zhong†
University of California, Los Angeles, Los Angeles, California 90095

DOI: 10.2514/1.J057775

There has been renewed interest in studying supersonic modes in hypersonic boundary layers. Recent computational results have shown supersonic modes in hot-wall flows, upending the notion that they exist only in cold-wall flows. Furthermore, supersonic modes with larger peak growth rates than the second mode have been encountered in a very blunt cone geometry. Therefore, conditions leading to supersonic modes and their dominant amplification must be thoroughly and systematically investigated. Specifically, the impact of wall temperature in high-enthalpy environments is of immediate interest. This work uses thermochemical nonequilibrium direct numerical simulation (DNS) and linear stability theory (LST) to simulate Mach 10 flow over a 1 mm nose radius axisymmetric cone. Despite LST results indicating no supersonic modes in either the hot- or cold-wall flow, DNS results indicate their presence in both cases, with the cold wall exciting the supersonic mode comparably to the second mode. Further fast Fourier transform analyses suggest that this was a result of the nonlinear interaction between an unstable subsonic mode S, stable supersonic mode F1, and the slow acoustic spectrum. Because the supersonic mode in the cold-wall case had a comparable growth rate to the second mode, the supersonic mode could impact transition unexpectedly if not accounted for.

Nomenclature

$\bar{a}$	=	mean sound speed, m/s
c_r	=	phase speed, m/s
f	=	frequency, kHz
$\bar{M}$	=	complex relative Mach number
M_∞	=	freestream Mach number
N	=	N-factor
p	=	pressure, kPa
s	=	streamwise distance, m; or species
T	=	translation–rotation temperature, K
T_V	=	vibration temperature, K
T_w	=	wall temperature, K
$\bar{u}$	=	mean tangential velocity, m/s
α_r	=	wave number, 1/m
$-\alpha_i$	=	growth rate, 1/m
ω	=	dimensional circular frequency
∞	=	freestream

I. Introduction

THE laminar–turbulent boundary-layer transition location in the hypersonic regime is of particular interest because of the drastically increased drag and heating associated with turbulent flow [1–3]. Thermal protection systems (TPSs) to defend against the high heat flux are often specified with a large factor of safety. Therefore, accurately modeling the mechanisms leading to transition can have a significant payoff in terms of the reduction of this factor of safety, reducing TPS weight, thereby enabling a larger vehicle payload.

The dominant instability mechanism leading to transition in the hypersonic regime at zero angle of attack with low environmental noise is Mack's second mode [4]. The second mode has been visualized as a trapped acoustic wave between the wall and the relative sonic line [1,3,5,6]; however, that description is only strictly valid under very particular and often unrealistic circumstances [6–8]. Specifically, the trapped acoustic wave only applies in the large-wave-number limit for a neutral disturbance. In reality, these assumptions are too restrictive, although the physical picture is qualitatively similar. Nevertheless, such a visualization is instructive to those performing direct numerical simulation (DNS) and experiments. A schematic for the second mode is shown in Fig. 1. Note the importance of the relative sonic line y_s, indicated by $\bar{M}(y_s) = -1$, where

$$\bar{M}(y) = \frac{\bar{u}(y) - c}{\bar{a}(y)}$$

where $\bar{u}(y)$ is the local mean flow velocity tangential to the wall, $c = \omega/\sqrt{\beta^2 + \alpha^2}$ is the disturbance propagation speed (with ω the circular frequency, β the spanwise wave number, and α the streamwise wave number), and $\bar{a}(y)$ is the local mean flow speed of sound. The disturbance propagation speed c is constant in the wall-normal direction for the entire disturbance structure at a fixed frequency and location. Between the sonic line and the wall, the disturbance is propagating downstream supersonically with respect to the mean flow velocity, resulting in the acousticlike behavior. Again, the acoustic description of the flow is only exact in very particular circumstances [6–8] but provides a qualitatively similar description of the flow in reality. Outside of the sonic line, the disturbance propagates subsonically. At the critical layer [$\bar{M}(y_c) = 0$], ropelike structures are observed both numerically [9–11] and experimentally [12,13]. Because the disturbance travels subsonically in the freestream [$\bar{M}(y) < 1$], the traditional second mode is referred to as a subsonic mode.

When the phase speed of the disturbance is supersonic with respect to the mean flow in the freestream [$\bar{M}(y) > 1$], the mode is known as a supersonic mode, and additional physical phenomena are encountered. A schematic similar to Fig. 1 is presented in Fig. 2 for the supersonic mode, which shows the same structures near the wall as the subsonic mode. Below the first sonic line [$\bar{M}(y_{s1}) = -1$], the disturbance propagates downstream supersonically with respect to the mean flow, and the critical layer [$\bar{M}(y_c) = 0$] is outside of this first sonic line. However, with the supersonic mode, a second relative sonic line is included [$\bar{M}(y_{s2}) = 1$], outside of which the disturbance travels upstream supersonically with respect to the mean flow. The three distinct regions (two supersonic, one subsonic) have also been described by Mack [6]. In the outer supersonic region, because there

Received 26 July 2018; revision received 2 October 2018; accepted for publication 16 November 2018; published online 28 December 2018.

*Graduate Student, Mechanical and Aerospace Engineering Department; carleton.knisely@gmail.com. Student Member AIAA.

†Professor, Mechanical and Aerospace Engineering Department; xiaolin@seas.ucla.edu. Associate Fellow AIAA.

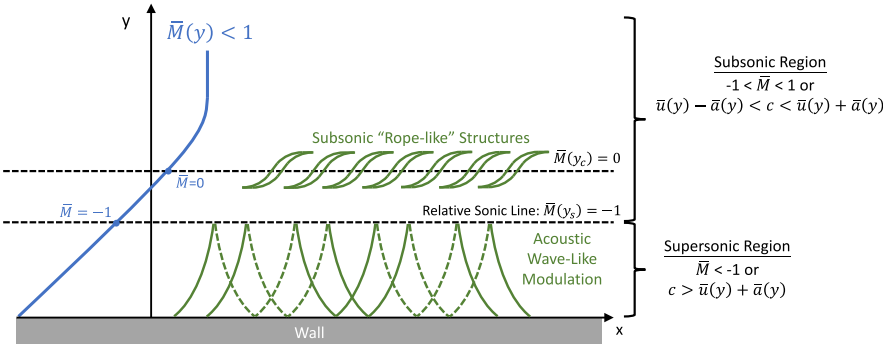

Fig. 1 Visualization of neutral second mode similar to [1,3,5,6] assuming large wave number. Reflection at the sonic line changes waves from compression to expansion and vice versa.

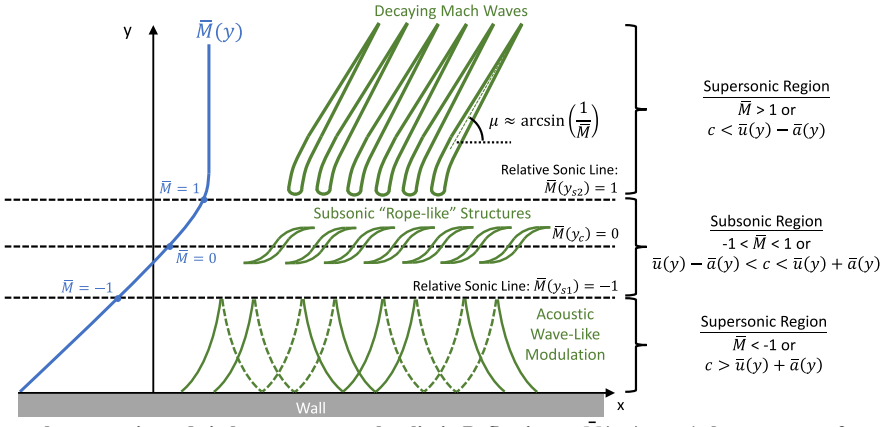

Fig. 2 Visualization of neutral supersonic mode in large-wave-number limit. Reflection at $\bar{M}(y_{s1}) = -1$ changes waves from compression to expansion and vice versa.

is no outer sonic line to reflect acoustic waves, the Mach-wave-like structures are formed and can be approximated by $\mu \approx \arcsin(1/\bar{M})$. For a neutral supersonic wave, this relation is exact. However, because a nonneutral wave will have an imaginary component of the wave number, the Mach wave angle for a nonneutral instability will have a slightly different angle. The Mach-wave-like structures visualized for the supersonic mode can be interpreted as acoustic radiation away from the boundary layer; therefore, the supersonic mode has also been referred to as the spontaneous radiation of sound [14]. Again, however, the description of acoustic radiation only applies to a neutral mode under the large-wave-number assumption [6–8]. In reality, the large-wave-number assumption is inaccurate, and there is an imaginary component of the wave number. Therefore, the decaying waves outside of the boundary layer are not exact acoustic waves but rather share qualitative characteristics to acoustic waves.

Despite the existence of the supersonic mode being known since the mid-1980s by Mack [6,15], Reshotko in the early 1990s [1], and Chang et al. in 1997 [16], the general consensus was that the supersonic mode is insignificant due to its smaller disturbance amplification rate than the second mode and because the supersonic mode is an artifact of highly cooled walls. Therefore, few studies have been performed directly analyzing the supersonic mode, although it has been encountered in many other studies [14,17–23]. Even with the recent resurgence in interest in the supersonic mode sparked by Bitter and Shepherd [24], most studies [25–30] have shown a weaker supersonic mode than the traditional second mode. However, based on Edwards and Tumin's [27] finding of the supersonic mode on a hot wall with chemical effects, the effect of wall temperature on the supersonic mode in thermochemical nonequilbrium flow must be reevaluated. Furthermore, Mortensen [31] discovered the supersonic mode in Mach 20 thermochemical nonequilibrium flow over very blunt cones and determined the supersonic mode to have a significantly higher sustained growth rate than the second mode for nose radii greater than approximately 36 mm. Such a finding is novel and raises concerns of a dominant supersonic mode existing in other seldom-studied (but still practically relevant) flows. Therefore, a comprehensive examination of the supersonic mode's impact on transition to turbulence must be performed.

The goals of this study are to contribute a small piece to the overall understanding of the supersonic mode through examining the effect of a hot wall versus a cold wall using thermochemical nonequilibrium DNS and linear stability theory (LST) analysis of a blunt (1-mm-radius) axisymmetric cone in high-enthalpy flow. Previous works by the authors have verified the LST and DNS are capable of capturing the supersonic mode [28] and verified the supersonic mode's existence in hot-wall high-enthalpy flow [29]. This work is a continuation of the authors' overall goal of determining the envelope of flow conditions leading to the supersonic mode and its impact on transition to turbulence. Specifically, here the impact of wall temperature ratio on the supersonic mode at high-enthalpy conditions is examined.

II. Simulation Conditions

The flow conditions for this study are summarized in Table 1 and are intended to be similar to those used by Edwards and Tumin [27]. The geometry is a 5 deg half-angle axisymmetric blunt cone 1 m in length with a nose radius of 1 mm. The DNS simulations used 256

Table 1 Flow conditions for DNS simulations

Parameter	Case 1	Case 2
M_∞	10	10
$H_{0,\infty}$, MJ/kg	14.78	14.78
ρ_∞, kg/m^3	1.91×10^{-2}	1.91×10^{-2}
p_∞, kPa	4	4
T_w, K	1000	300
T_w/T_∞	1.43	0.43

points in the wall-normal direction and roughly five points per millimeter on the surface of the cone in the streamwise direction. In the azimuthal direction, four points are used. LST simulations interpolated the DNS mean flow onto the LST grid defined by the stretching methods discussed in the following sections.

As will be explained in the following sections, the DNS code used in this study uses a shock-fitting method. Thus, the parameters in Table 1 are the freestream conditions upstream of the shock formed over the body. It should be noted that the wall temperatures in both case 1 and case 2 are less than the adiabatic wall temperature. However, as Bitter and Shepherd [24] have shown, the wall temperature ratio with respect to the boundary-layer edge temperature is an important parameter affecting the supersonic mode. Therefore, case 1 is denoted a "hot wall" because the wall temperature is greater than the boundary-layer edge temperature. Similarly, case 2 is a "cold wall" because the wall temperature is less than the boundary-layer edge temperature.

III. Governing Equations and Gas Model

The governing equations for the DNS and LST codes are those developed by Mortensen and Zhong [32–36] and Mortensen [37], which are formulated for thermochemical nonequilibrium assuming a two-temperature model. Their formulation is highlighted here for clarity. The rotational mode is assumed to be fully excited with up to 11 nonionizing species with finite-rate chemistry. Two temperatures are used to represent translation–rotation energy and vibration energy. There are two species models: an 11-species model (N_2, O_2, NO, C_3, CO_2, C_2, CO, CN, N, O, and C) used for ablation studies and a five-species model (N_2, O_2, NO, N, and O) used to simulate air. The five-species model is used here. The Navier–Stokes equations in conservative form consist of five species mass conservation equations, three momentum conservation equations, the total energy equation, and the vibration energy equation. The governing equations in vector form are written as

$$\frac{\partial U}{\partial t} + \frac{\partial F_j}{\partial x_j} + \frac{\partial G_j}{\partial x_j} = W \tag{1}$$

where U is the state vector of conserved quantities, W is the source terms, and F_j and G_j are the inviscid and viscous flux vectors, respectively. For further details of the governing equations and thermochemical model, see the work of Knisely and Zhong [28–30] and Mortensen [37].

IV. Numerical Methods

A. Direct Numerical Simulation

The thermochemical nonequilibrium code developed by Mortensen and Zhong [32–36] and Mortensen [37] uses a fifth-order upwind explicit shock-fitting method to compute the flowfield between the shock and the body. The numerical method is not repeated here for brevity. For shock-fitting computations, the shock location is not known a priori, and so its position is solved along with the flowfield. Because the shock position is not stationary, the grid used to compute the flowfield is a function of time.

Conditions behind the shock are calculated from Rankine–Hugoniot relations. In the freestream, the flow is assumed to be in thermal equilibrium, and the chemical composition of the flow is frozen. The shock is assumed to be infinitely thin, which means that the flow has no time to relax as it crosses the shock because relaxation rates are finite. This leads to the chemical composition remaining constant across the shock as well as the vibration temperature. Because neither process has any time to relax across the shock, the relaxation zone is entirely downstream of the shock. A complete derivation of thermochemical nonequilibrium shock fitting can be found in Prakash et al. [38]. A low-storage first-order Runge–Kutta method from Williamson [39] is used to advance the solution in time.

B. Linear Stability Theory

The linear stability analysis used here is largely based on the LST code developed by Mortensen [37]; however, here the assumption of zero wall-normal velocity is relaxed (i.e., $\bar{v} \neq 0$), and freestream boundary conditions incorporating a shock at the computational boundary are used. The modified LST code has been verified by Knisely and Zhong [28]. The LST equations are derived from the governing equations [Eq. (1)], in which the instantaneous flow is composed of a mean and fluctuating component. The instantaneous flow is then substituted into the governing equations, in which the steady flow is assumed to satisfy the governing equations and is subtracted out. The mean flow is assumed to be a function of y only, and the flow disturbances are assumed to be small (i.e., linear). The perturbations are then assumed to be in the form of a normal mode described by $q' = \hat{q}(y)\exp[i(\alpha x + \beta z - \omega t)]$, in which ω is the circular frequency of the disturbance, and α and β are the wave numbers. For comparison to direct numerical simulation, the spatial stability approach is used, i.e., α is complex, which results in the dispersion relation $\alpha = \Omega(\omega, \beta)$. Substituting in the normal mode form for the perturbation reduces the problem for a species model with ns species to a coupled set of $ns + 5$ ordinary differential equations:

$$\left(\boldsymbol{A}\frac{d^2}{dy^2} + \boldsymbol{B}\frac{d}{dy} + \boldsymbol{C}\right)\boldsymbol{\phi} = 0 \tag{2}$$

where $\boldsymbol{\phi} = [\hat{\rho}_1, \hat{\rho}_2, \ldots, \hat{\rho}_{ns}, \hat{u}, \hat{v}, \hat{w}, \hat{T}, \hat{T}_V]^T$, and $\boldsymbol{A}$, $\boldsymbol{B}$, and $\boldsymbol{C}$ are complex square matrices of size $ns + 5$. This is now a boundary-value problem, in which the derivative operators can be discretized and the equations solved numerically.

For hypersonic compressible boundary layers, it is important to have high grid resolution near the generalized inflection point [4]. The grid used here clusters points around the inflection point and near the wall and more evenly distributes points in the freestream [28] to capture the oscillatory behavior of the supersonic mode eigenfunctions. Structuring the grid in such a way retains the benefits of capturing the sharp increases in eigenfunctions at the wall and at the generalized inflection point, while adding additional resolution in the freestream and near the outer edge boundary.

With the grid defined, Eq. (2) can be transformed into computational space, and a numerical representation of the derivatives can be given. The first and second derivative operators in the wall-normal direction are discretized by taking derivatives of Lagrange polynomials in physical space. Here, a five-point stencil is used, resulting in a fourth-order method similar to the one used by Malik [40].

After discretization, nonlinearities exist in α, and so the global method suggested by Malik [40] is used to compute the eigenvalue spectrum with $\alpha^2 = 0$. This method computes the eigenvalues from a generalized eigenvalue problem $\tilde{A}\boldsymbol{\phi} = \alpha\tilde{B}\boldsymbol{\phi}$, where the LAPACK [41] subroutine ZGGEV is used here for solution. From the eigenvalue spectrum, an initial guess can be obtained for the local method, which results in $\bar{A}\boldsymbol{\phi} = \bar{B}$, and the eigenvalue is found iteratively without dropping the α^2 terms. The LAPACK subroutine ZGESV is used to solve the local problem. It is also possible to avoid the computationally intensive global method and obtain an initial guess for α from a nearby streamwise location or a DNS simulation, assuming that the unsteady DNS results are available.

Boundary conditions are required for the freestream and the wall. The wall boundary conditions at the wall are a noncatalytic high-order pressure extrapolation condition, assuming zero mass flux from the wall and zero temperature perturbation for both temperatures, although more complex surface boundary conditions can be used for ablation studies [33,37]. In the freestream, the shock boundary conditions developed by Knisely and Zhong [28] are used.

LST gives information about what disturbance frequencies are unstable and the corresponding growth rates of those frequencies, but there is no information on the amplitude of the incoming disturbance. To estimate boundary-layer transition using LST, the e^N transition criterion is used, which is defined as

$$e^N = \frac{A(s)}{A_0} = \exp\left[\int_{s_0}^{s} -\alpha_i(s,f)\,\mathrm{d}s\right] \tag{3}$$

where $A(s)$ is the integrated disturbance amplitude, A_0 is the initial disturbance amplitude, s_0 is the location where the disturbance first becomes unstable, and α_i is the spatial amplification rate obtained from LST. The integration is performed for a constant frequency f and is done numerically using trapezoidal integration. Note that a negative imaginary part of the wave number α results in disturbance growth, whereas a positive value results in disturbance decay. The N-factor is specifically the exponent of e^N. In-flight transition N-factors are commonly understood to be around 10. Malik [42] showed that 9.5 and 11.2 correlated with transition onset for two high-Mach-number flight tests. In ground-test facilities, the transition N-factor is usually lower.

V. Steady Direct Numerical Simulation Results

A. Case 1 Steady Direct Numerical Simulation Results

Steady DNS translation–rotation temperature, vibration temperature, and mass fraction contours for the nose region of the cone in case 1 are shown in Fig. 3. The upper half of Fig. 3a is translation–rotation temperature T, and the lower half is vibration temperature T_V. Figure 3a indicates that the flow is in thermal nonequilibrium in the nose region. Similarly, the mass fractions of N_2 and O_2 are shown in the upper and lower halves of Fig. 3b, respectively. Figure 3b indicates that the flow is in chemical nonequilibrium. Specifically, O_2 dissociation is the predominant reaction in this flowfield, whereas N_2 does not dissociate as severely.

Farther downstream, the nonequilibrium effects weaken; however, there is still significant vibrational and chemical effects. Figure 4 shows the boundary-layer profiles for temperature, vibration temperature, tangential velocity, and species density of N_2 and O_2 at a streamwise distance from the stagnation point of $s = 0.4$, far downstream of the region shown in Fig. 3. Hereafter, y denotes the wall-normal distance, and u denotes the component of velocity tangential to the surface of the cone. The mean flow does not reach thermal equilibrium in the freestream, and the species densities of N_2 and O_2 species vary in the freestream, thus demonstrating the necessity of accounting for nonequilibrium effects in these types of flows.

B. Case 2 Steady Direct Numerical Simulation Results

The steady DNS translation–rotation temperature, vibration temperature, and mass fraction contours for the nose region of the cone for case 2 are shown in Fig. 5. Similar nonequilibrium effects occur in case 2 as in case 1 because only the wall temperature is varied. Figure 5a indicates that the flow is in thermal nonequilibrium in the nose region, and Fig. 5b indicates that the flow is in chemical nonequilibrium. Again, O_2 dissociation is the predominant reaction in this flowfield, whereas N_2 does not dissociate as severely.

Farther downstream, the boundary-layer profiles (Fig. 6) indicate that case 2 is in thermal nonequilibrium in the freestream, similar to the previous case. However, the species densities of N_2 and O_2 appear to change in magnitude much more than in case 1, suggesting that chemical effects play a larger role near the wall due to the cold wall in case 2.

VI. Linear Stability Theory Results

For both case 1 and case 2 the freestream values used in nondimensionalizing the LST results were $u^*_\infty = 5303$ m/s,

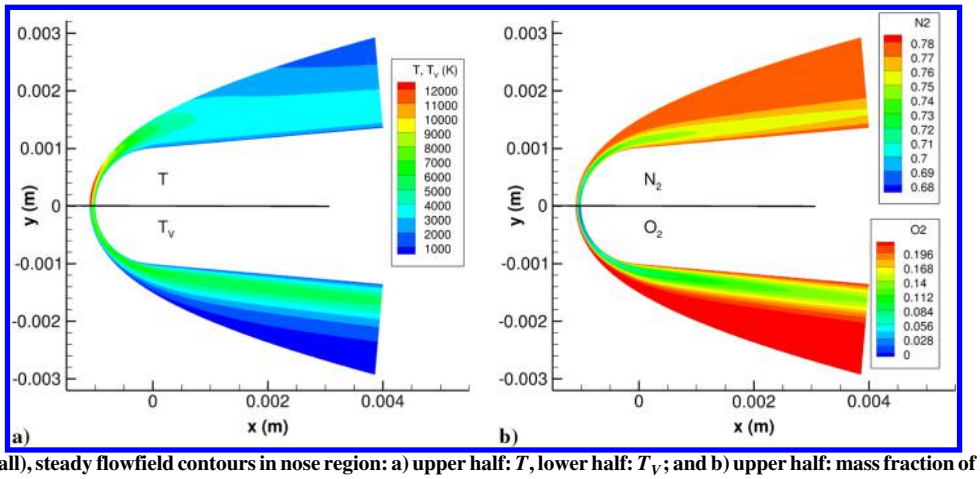

Fig. 3 Case 1 (hot wall), steady flowfield contours in nose region: a) upper half: T, lower half: T_V; and b) upper half: mass fraction of N_2, lower half: mass fraction of O_2.

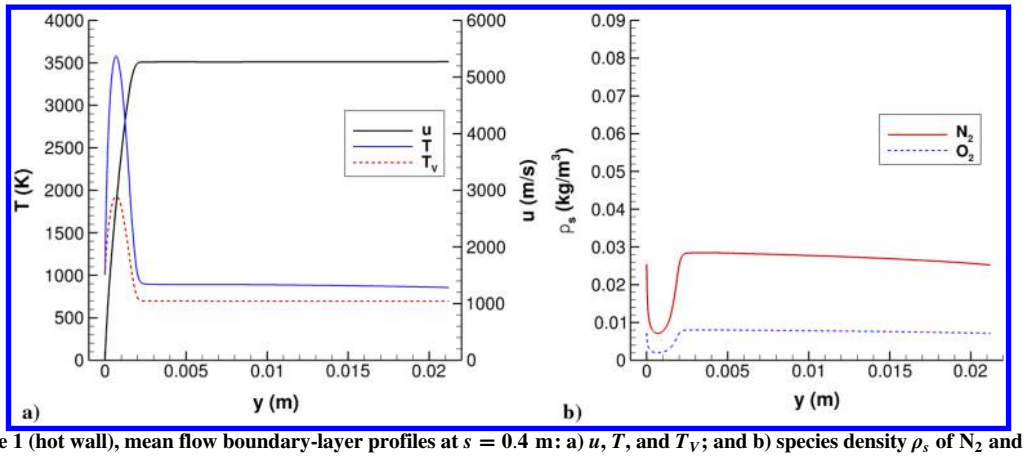

Fig. 4 Case 1 (hot wall), mean flow boundary-layer profiles at $s = 0.4$ m: a) u, T, and T_V; and b) species density ρ_s of N_2 and O_2 species.

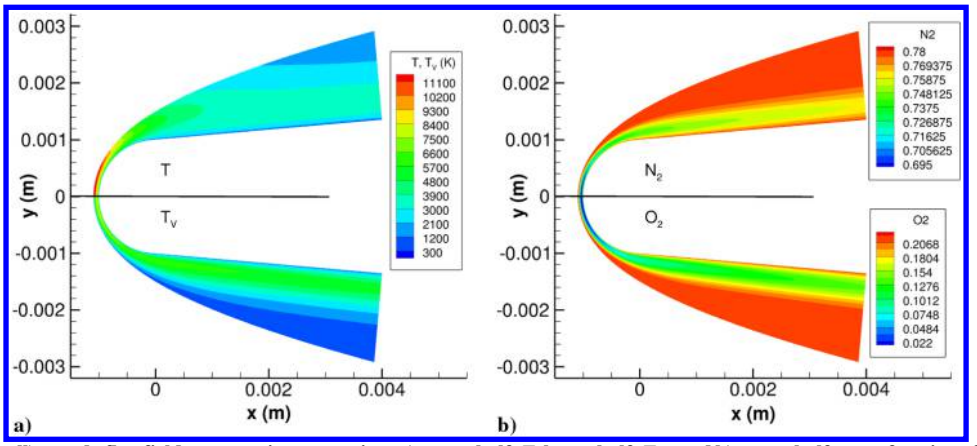

Fig. 5 Case 2 (cold wall), steady flowfield contours in nose region: a) upper half: T, lower half: T_V; and b) upper half: mass fraction of N_2, lower half: mass fraction of O_2.

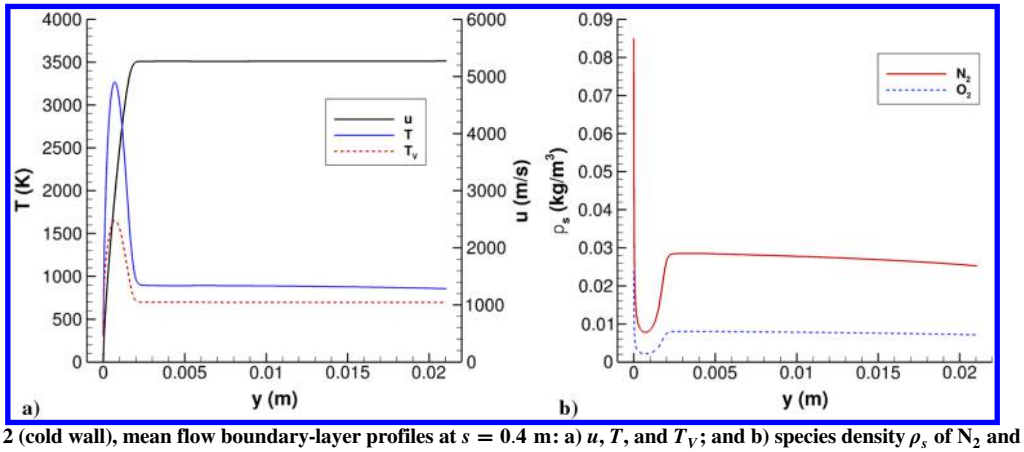

Fig. 6 Case 2 (cold wall), mean flow boundary-layer profiles at $s = 0.4$ m: a) u, T, and T_V; and b) species density ρ_s of N_2 and O_2 species.

$\rho^*_\infty = 0.01991\,\text{kg/m}^3$, and $\mu^*_\infty = 3.320 \times 10^{-5}$ (kg · m)/s, in which the nondimensional phase speed is defined as

$$c_r = \frac{(\omega^*/u^*_\infty)}{\sqrt{\beta^2 + \alpha_r^2}}$$

where $\omega^* = 2\pi f$ is the dimensional circular frequency, and u^*_∞ is the freestream velocity upstream of the shock.

The nomenclature for hypersonic boundary-layer instability modes has evolved throughout the decades, and so it is pertinent to describe the first and second modes with respect to Fedorov and Tumin's [43] contemporary notation using mode F1 and mode S in conjunction with the continuous modes: the fast and slow acoustic, entropy, and vorticity spectra. Mode S and mode F1 are discrete modes that originate in the slow and fast acoustic spectra, respectively, at the leading edge of the body. The first mode is a viscous instability and occurs when mode S has an unstable region before synchronization with mode F1. Synchronization is defined as two modes having the same phase speed, regardless of growth rate. The first mode is the compressible analog of Tollmien–Schlichting waves, and in hypersonic flows, the first mode can be completely stabilized with increasing Mach number. The second mode is an inviscid instability and occurs downstream of synchronization of mode S with mode F1. Either mode S or mode F1 can become unstable after synchronization while the other is stabilized [43]. Farther downstream on the body, the higher-frequency modes F2, F3, etc., behave similar to mode F1 and can synchronize with mode S, leading to the third, fourth, and higher Mack modes. However, the third and higher modes are decreasing in amplitude from the second mode [4]; therefore, the focus of the majority of hypersonic boundary-layer transition studies is on the second mode.

A. Case 1 Linear Stability Theory Results

Linear stability theory (LST) calculations for case 1 were performed by Knisely and Zhong [29]; some important results are highlighted here. The phase speed and growth rate curves for $f = 600$ kHz are shown in Fig. 7. LST predictions indicated a stable mode F1 and an unstable mode S for case 1, meaning that there was no unstable supersonic mode expected because the mode S phase speed does not go below the slow acoustic wave speed $c_r = 1 - 1/M_\infty$. It should be noted that the discontinuity in mode F1 is due to the LST solver not resolving the discrete mode in the vicinity of the entropy/vorticity spectra near $c_r = 1$. Because of the iterative method of solution, the discrete mode gets "lost" in the continuous spectrum. However, the solver is still able to resolve the mode S and mode F1 synchronization location near $s = 0.5$ m.

For a complete picture of the second mode, the stability of mode S for a range of frequencies over the entire length of the cone was computed, resulting in the neutral stability map for mode S (Fig. 8a). The neutral stability map indicates the locations and frequencies at which mode S is unstable. The region of instability of the second mode is the area inside the thick black curve. At the lowest frequencies and near the nose of the cone (left-hand side of Fig. 8a), the numerical solver is not stable, and a physical solution is not obtained. The maximum overall growth rate occurs at approximately $s = 0.24$ m at a frequency of $f = 840$ kHz. Because mode S is the unstable mode for these conditions, there can exist higher modes that are amplified. Specifically, the third mode is apparent in the upper-right corner of Fig. 8a. The third mode is visible after the synchronization of mode F2 with mode S; however, the synchronization is not sufficient to make the third mode unstable. The second mode is significantly more amplified and is the predicted cause of transition. To relate the mode S instability to empirical estimates of transition to turbulence, the N-factor curve

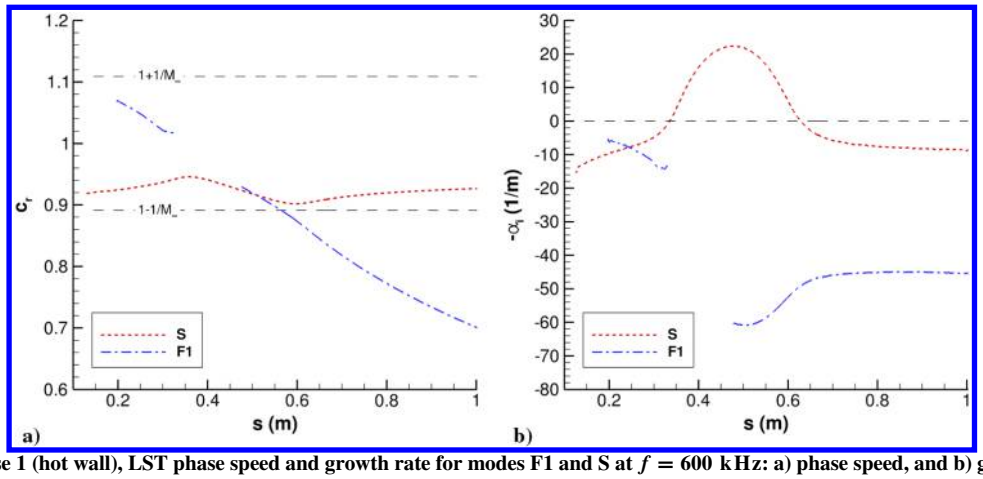

Fig. 7 Case 1 (hot wall), LST phase speed and growth rate for modes F1 and S at $f = 600$ kHz: a) phase speed, and b) growth rate.

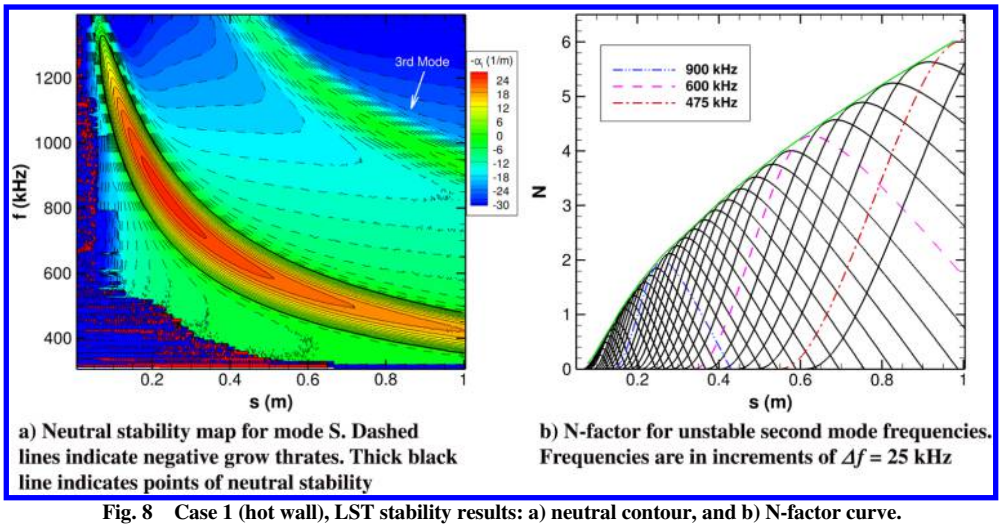

a) Neutral stability map for mode S. Dashed lines indicate negative grow thrates. Thick black line indicates points of neutral stability

b) N-factor for unstable second mode frequencies. Frequencies are in increments of $\Delta f = 25$ kHz

Fig. 8 Case 1 (hot wall), LST stability results: a) neutral contour, and b) N-factor curve.

was calculated, shown in Fig. 8b. A maximum N-factor of approximately 6 due to a frequency of $f = 475$ kHz is achieved by the end of the 1-m-long cone.

B. Case 2 Linear Stability Theory Results

The phase speed and growth rate curves for case 2 at $f = 700$ kHz are shown in Fig. 9. LST predictions indicate a stable mode F1 and an unstable mode S for case 2, similar to case 1. Again, this means that there is no unstable supersonic mode expected because the mode S phase speed does not go below the slow acoustic wave speed $c_r = 1 - 1/M_\infty$.

The neutral stability map for mode S (Fig. 10a) was computed for case 2. Because of the cold wall destabilizing mode S, the third mode is actually unstable in case 2, whereas it was stable in case 1. However, the third mode amplitude is significantly weaker than the second mode, and therefore the second mode is still the predicted cause of transition. The regions of instability of the second and third modes are the areas inside the thick black curves. The overall maximum growth rate occurs at approximately $s = 0.25$ m at a frequency of $f = 860$ kHz. The second-mode instability leads to an N-factor of approximately 5 by the end of the 1-m-long cone (Fig. 10b).

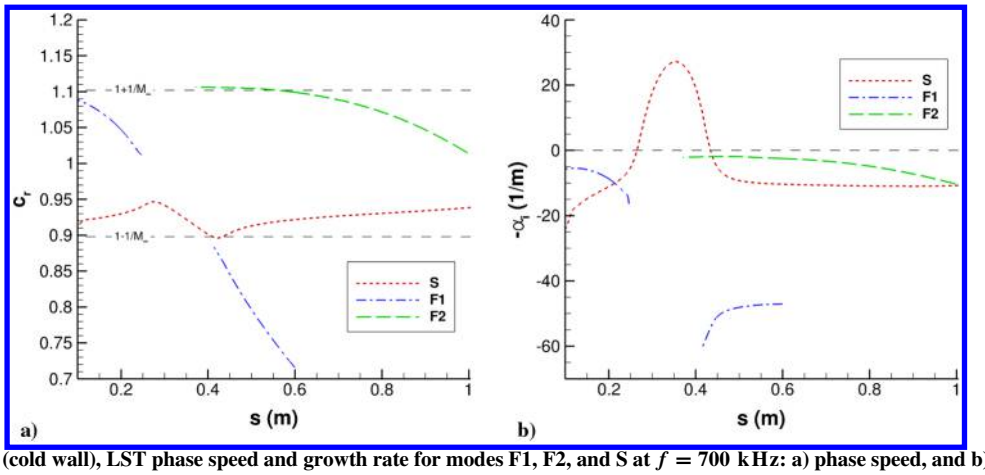

Fig. 9 Case 2 (cold wall), LST phase speed and growth rate for modes F1, F2, and S at $f = 700$ kHz: a) phase speed, and b) growth rate.

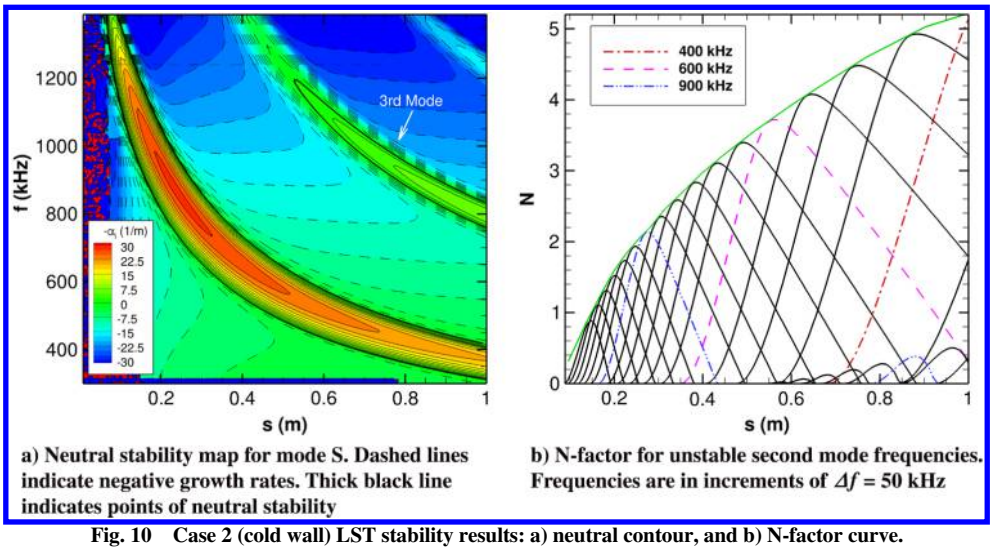

a) Neutral stability map for mode S. Dashed lines indicate negative growth rates. Thick black line indicates points of neutral stability

b) N-factor for unstable second mode frequencies. Frequencies are in increments of $\Delta f = 50$ kHz

Fig. 10 Case 2 (cold wall) LST stability results: a) neutral contour, and b) N-factor curve.

VII. Unsteady Direct Numerical Simulation Results

To study stability using DNS, it is required that the mean flow be perturbed to study the growth, or decay, of the perturbation. Here, the flow is perturbed with a suction/blowing slot at the cone surface. The equation for the mass flux of the slot is

$$\rho v(x,t)'_w = \epsilon_b (\rho u)_\infty \exp\left\{-\frac{(t-\mu_b)^2}{2\sigma_b^2}\right\} \sin\left\{\frac{2\pi(x-x_b)}{l_b}\right\} \qquad (4)$$

where l_b is the length of the slot, x_b is the center of the slot measured from the leading edge of the cone, ϵ_b scales the function, μ_b shifts the Gaussian component to avoid negative times, and σ_b adjusts the spectral content of the function. Notice the time-dependent Gaussian portion of the function. When transformed to frequency space, this yields a continuous range of frequencies with nonzero amplitudes, making this particular approach for perturbing the mean flow an effective strategy when studying a wide range of frequencies.

The parameters for the unsteady pulse, given by Eq. 4, are summarized in Table 2. The Gaussian pulse and its Fourier transform (Fig. 11) show the majority of the frequency content if the pulse is below 1.2 MHz. The same pulse parameters are used for case 1 and case 2.

Table 2 Gaussian pulse parameters for unsteady DNS

ϵ_b	μ_b	σ_b	x_b	l_b
$1E-4$	$3E-6$	$3E-7$	0.1 m	0.002 m

A. Case 1 Unsteady Direct Numerical Simulation Results

The evolution of the Gaussian pulse in case 1 is visualized in Fig. 12 using snapshots in time of contours of the pressure perturbation normalized by the local mean flow pressure ($\Delta p/p$). The same value at the surface of the cone is included to more clearly visualize the growth of disturbances. The traditional second-mode growth can be seen in Fig. 12a between $x = 0.65$ and $x = 0.7$ m. However, contrary to the LST predictions, the start of the spontaneous radiation of sound appears in Fig. 12a for $x < 0.65$ m. When the pulse travels farther downstream, the spontaneous radiation of sound becomes much more apparent, shown in Fig. 12b. In particular, the sound radiation is shown very clearly between $x = 0.73$ m and $x = 0.87$ m. Further Fourier decomposition analysis is required to determine whether or not this sound radiation is an artifact of the supersonic mode. Fast Fourier transform (FFT) enables computation of the disturbance phase speed and growth rate, which can be compared to LST. Furthermore, for a fixed frequency, an eigenfunction can be computed from the DNS and compared to LST eigenfunctions. A combination of these methods can be used to identify qualitatively the modal composition of the disturbance in the absence of a multimode decomposition technique.

An FFT was performed on the time history of the surface pressure perturbation at all streamwise locations, resulting in the contour map in Fig. 13a. This contour shows the most unstable excited frequencies due to the Gaussian pulse. The neutral stability curve predicted by LST from Fig. 8a is overlaid in Fig. 13a for comparison. The most amplified frequency from the Gaussian pulse is approximately $f = 475$ kHz and appears most prominently for $s > 0.95$ m. This result agrees remarkably well with the N-factor results from LST. The FFT results follow the LST predictions reasonably closely, despite the absence of the radiation of sound in the LST results. It is likely that

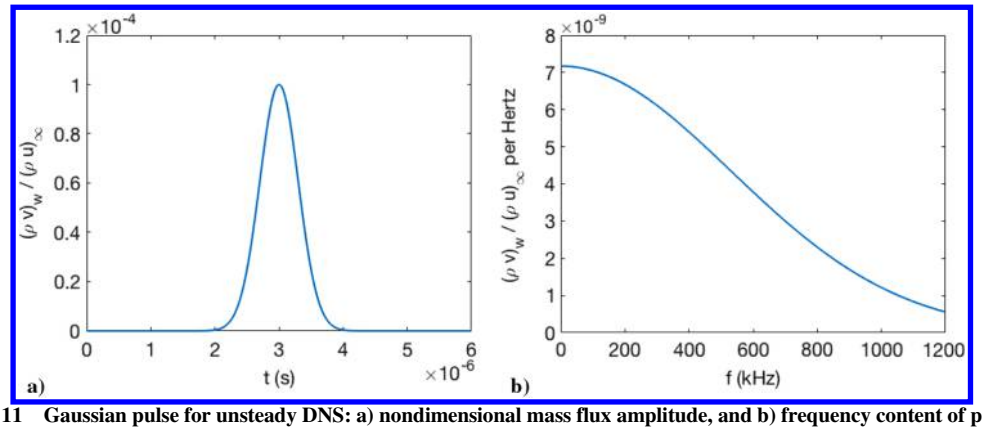

Fig. 11 Gaussian pulse for unsteady DNS: a) nondimensional mass flux amplitude, and b) frequency content of pulse.

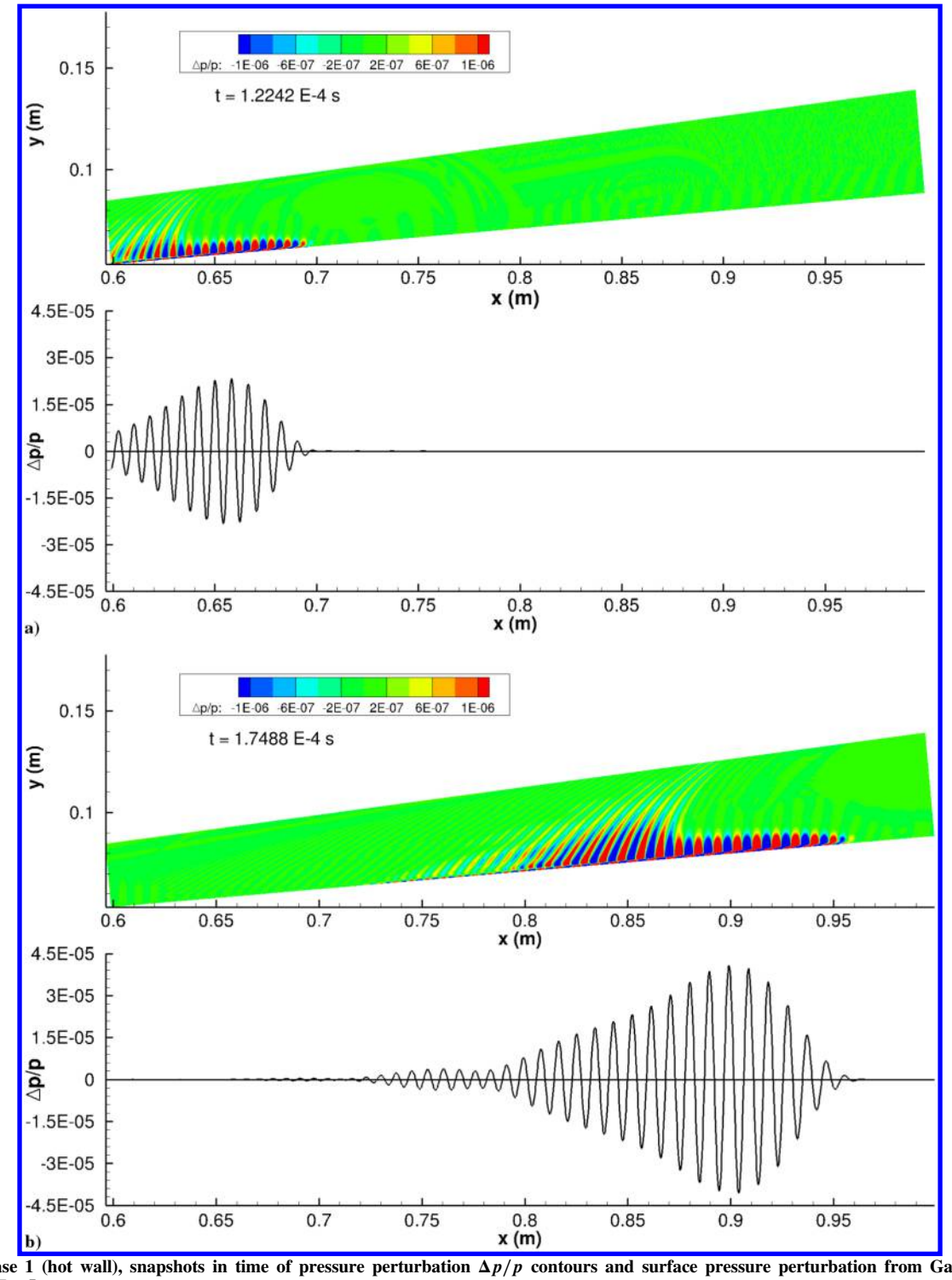

Fig. 12 Case 1 (hot wall), snapshots in time of pressure perturbation $\Delta p/p$ contours and surface pressure perturbation from Gaussian pulse. $\Delta t = 5.246E-5s$.

the amplitude of the supersonic mode is relatively weak in this flow, and the traditional second mode is the dominant instability.

It is useful to compare the FFT results to those obtained by Chuvakhov and Fedorov [25] for a cold-wall flat plate. Although the wall temperature ratio and blowing/suction slot are different from those of the current study, similar trends are observed for their supersonic mode. The Fourier transform of the unsteady pressure perturbation versus frequency for fixed streamwise locations is shown in Fig. 13b. Near the blowing/suction actuator ($s \leq 0.201$ m), the curve shape is similar to a bell curve. However, as the pulse travels downstream, the frequency content shifts and becomes asymmetrical. At each location $s \geq 0.252$ m, there is a dominant peak with at least one smaller amplitude peak occurring at a higher frequency than the dominant frequency. Chuvakhov and Fedorov [25] also obtained similar results for their study, in which they noted that, rather than the typical bell-shaped curves, multiple peaks are formed. Chuvakhov and Fedorov [25] observed three peaks at most in their FFT, which largely agrees with the results presented in Fig. 13b.

It is possible to determine the growth rate and phase speed of an unsteady disturbance in DNS. The Fourier decomposed perturbation variables can be used to reconstruct the perturbation flowfield via

$$\phi'(x, y, t) = \Delta\phi(x, y) \exp[i(\psi(x, y) - 2\pi f t)] \tag{5}$$

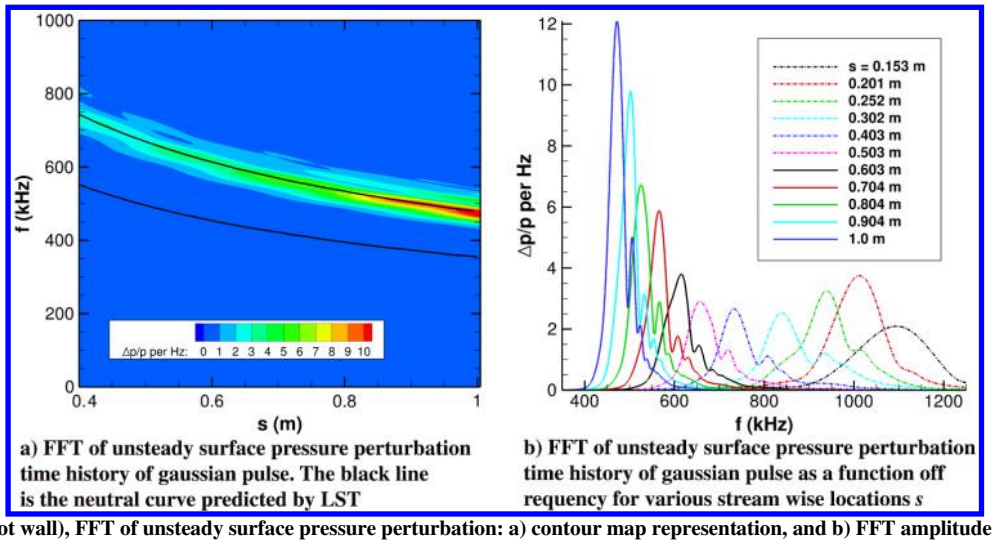

a) FFT of unsteady surface pressure perturbation time history of gaussian pulse. The black line is the neutral curve predicted by LST

b) FFT of unsteady surface pressure perturbation time history of gaussian pulse as a function off requency for various stream wise locations s

Fig. 13 Case 1 (hot wall), FFT of unsteady surface pressure perturbation: a) contour map representation, and b) FFT amplitude as a function of f.

where ϕ' is the perturbation of some variable, $\Delta\phi$ is the amplitude of that variable, ψ is the corresponding phase angle, and f represents a single dimensional frequency. The response of the entire flowfield for a particular frequency as a result of the unsteady pulse can be given directly by Eq. (5), provided that FFT data are available for all data points in the flowfield.

The FFT of the entire flowfield was performed and is shown in Fig. 14 for 700 kHz. There is a clear extension of the disturbance outside of the boundary layer, which is typical of the supersonic mode. The onset of the radiation into the freestream for $f = 700$ kHz is near $x = 0.35$ m. For the $f = 700$ kHz frequency, there is a clear amplification in the freestream for $x > 0.7$ m, whereas there is very little amplification near the wall in this region.

Multiple boundary-layer modes are present simultaneously in DNS; however, as one mode becomes dominant, it is possible to derive growth rate, wave number, and phase speed equations for a given frequency f from Eq. (5), resulting in

$$-\alpha_i = \frac{1}{\Delta\phi(f)}\frac{d}{ds}\Delta\phi(f) \tag{6}$$

$$\alpha_r = \frac{d}{ds}\psi(f) \tag{7}$$

$$c_r = \frac{2\pi f}{\alpha_r} \tag{8}$$

where s is the streamwise coordinate, $\Delta\phi(f)$ represents a variable amplitude at frequency f, and $\psi(f)$ represents the corresponding phase angle at frequency f. Similar to previous researchers [44], the surface pressure perturbations from DNS are used to compute $-\alpha_i$ and c_r.

The phase speed and growth rate calculated from DNS are compared to the LST predictions for a frequency of $f = 700$ kHz in Fig. 15. The DNS matches the LST predictions reasonably well, with a few areas of exception. The DNS and LST mode S results are similar in the region $0.35 < s < 0.4$ m due to mode S being the dominant mode, although the DNS phase speed is slower than that predicted by LST, and the DNS growth rate is larger than that predicted by LST. Downstream of $s = 0.45$ m, the DNS results oscillate about the LST mode S predictions for both phase speed and growth rate. This oscillatory behavior is the result of multiple modes existing simultaneously in the DNS simulation that are ignored in LST. However, the agreement between DNS and LST is still strong, considering the largely different methods used to obtain the results.

This extension of the disturbance into the freestream is typical of the supersonic mode. However, upon closer inspection of the growth rate, phase speed, and eigenfunctions of the DNS results, it is apparent that the dominant mode S is not the cause of the sound radiation. Rather, it is the collective nonlinear interaction of mode S, mode F1, and the slow acoustic spectrum that causes the supersonic mode in this case.

The eigenfunctions between LST and DNS can be compared to determine qualitatively the presence of multiple modes. The pressure eigenfunctions at $f = 700$ kHz were compared to the LST mode S, mode F1, and mode F2 predictions at different streamwise locations, shown in Fig. 16. Locations for eigenfunction comparison were selected to be just downstream of the synchronization of mode S with mode F1 ($s = 0.35$ m) and in the region where $c_r < 1 - 1/M_\infty$ ($s = 0.45$ m). The third location was selected based on Fig. 14, in which there are two distinct wall-normal locations of amplification

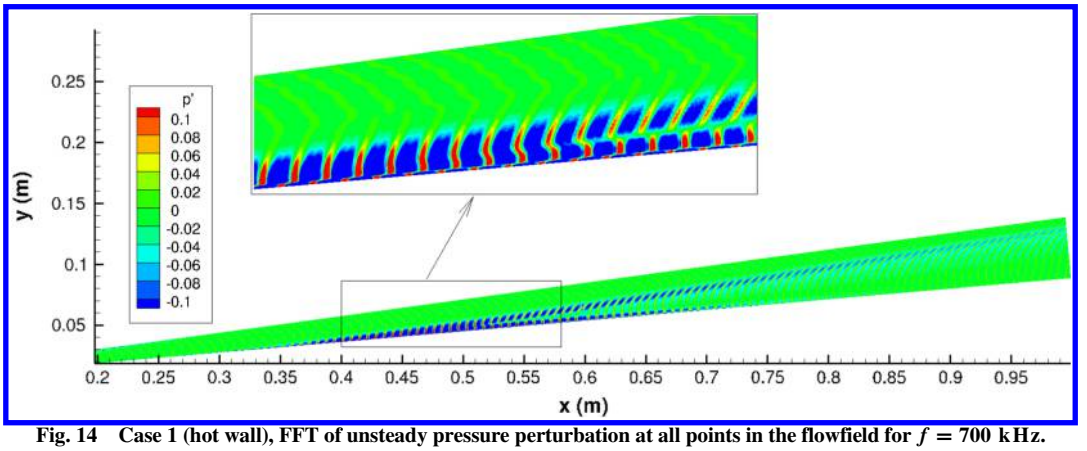

Fig. 14 Case 1 (hot wall), FFT of unsteady pressure perturbation at all points in the flowfield for $f = 700$ kHz.

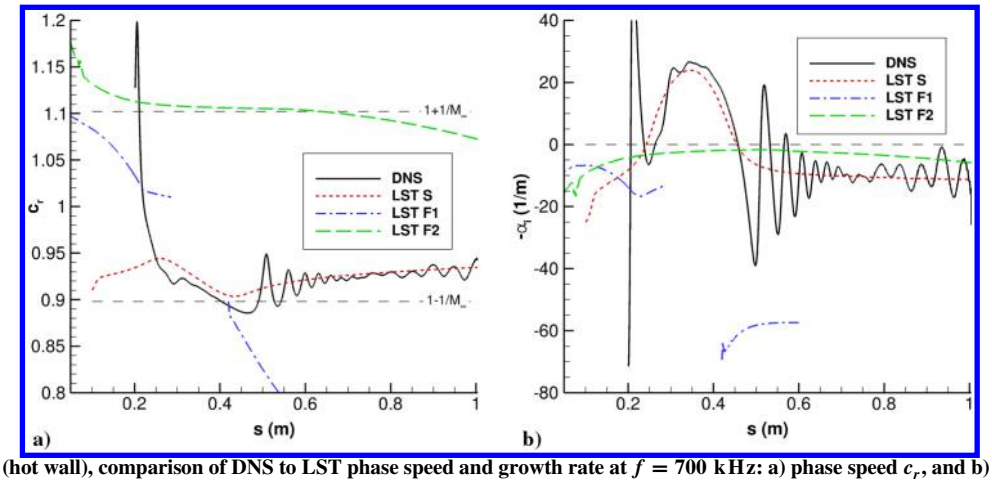

Fig. 15 Case 1 (hot wall), comparison of DNS to LST phase speed and growth rate at $f = 700$ kHz: a) phase speed c_r, and b) growth rate $-\alpha_i$.

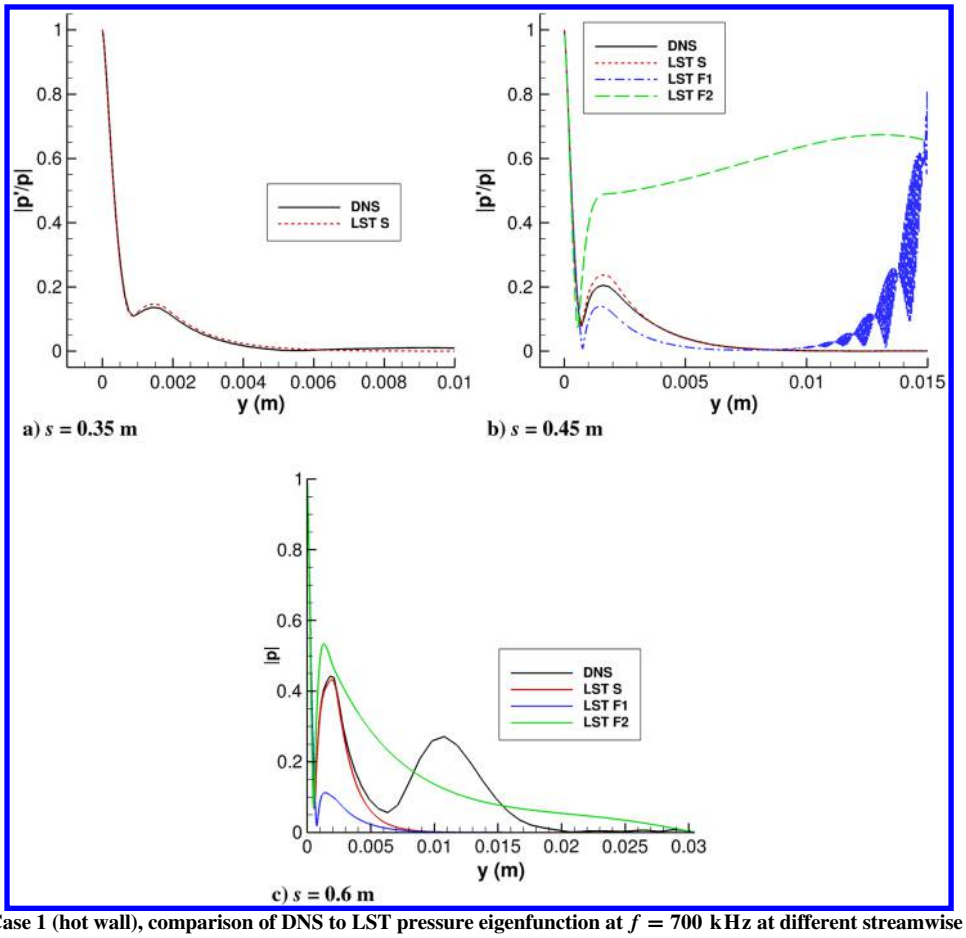

Fig. 16 Case 1 (hot wall), comparison of DNS to LST pressure eigenfunction at $f = 700$ kHz at different streamwise locations.

($s = 0.6$ m). At $s = 0.35$ m, the synchronization of mode S with mode F1 causes minimal oscillatory behavior in the freestream. The DNS pressure eigenfunction is a close match to the LST mode S prediction, suggesting the dominance of mode S in the flow at this location. At $s = 0.45$ m, the DNS phase speed is supersonic ($c_r < 1 - 1/M_\infty$); however, the DNS and LST mode S eigenfunctions do not exhibit any oscillatory behavior outside the boundary layer. Mode F1, however, exhibits strongly oscillatory behavior in the freestream due to its proximity to the slow acoustic spectrum, but nevertheless it is predicted to be stable. Furthermore, the DNS eigenfunction qualitatively lies between the LST mode S and mode F1 eigenfunctions, suggesting a contribution of mode F1 to the disturbance that did not exist upstream. Because mode F1 was not able to be resolved between $0.3 < s < 0.4$ m, it is possible that the interaction of the unstable mode S, stable mode F1, and slow acoustic spectrum cause a nonlinear excitation of the disturbance, resulting in the brief radiation of sound shown in Fig. 14. This interaction is similar to the interaction of mode F1 or mode F2 and the fast acoustic spectrum discussed by Ma and Zhong [44–46]. When the phase speed of the acoustic mode and the stable discrete mode are nearly equal, a resonant interaction can occur. Although the boundary-layer modes are stable, this interaction can cause the disturbance to amplify. Rather than causing the mode to become unstable, the resonant interaction acts as a source/forcing term, which is neglected in LST. Therefore, the supersonic mode is found in DNS due to the brief resonant interaction between mode S, mode F1, and the slow acoustic spectrum acting as a forcing term to the disturbance.

At $s = 0.45$ m, the mode S and DNS growth rates are near zero, and no significant unstable supersonic mode S exists. Interestingly, however, the eigenfunction at $s = 0.6$ m displays a clear second peak that is not predicted by LST, despite a subsonic phase speed and a negative growth rate. It is possible that this behavior in DNS is the result of the brief radiation of sound upstream of this location. In other words, it is likely that, somewhere between $0.3 < s < 0.4$ m, there is a modal energy exchange causing a resonant amplification of the stable mode F1 disturbance. This interaction acts as a source term and causes sound to radiate away from the wall. The sound radiation outside of the boundary layer continues to travel downstream, and its amplitude becomes slowly damped. Near the wall, however, the resonant interaction quickly ceases, mode F1 is stable, and mode S becomes stable as well, causing the disturbance amplitude to

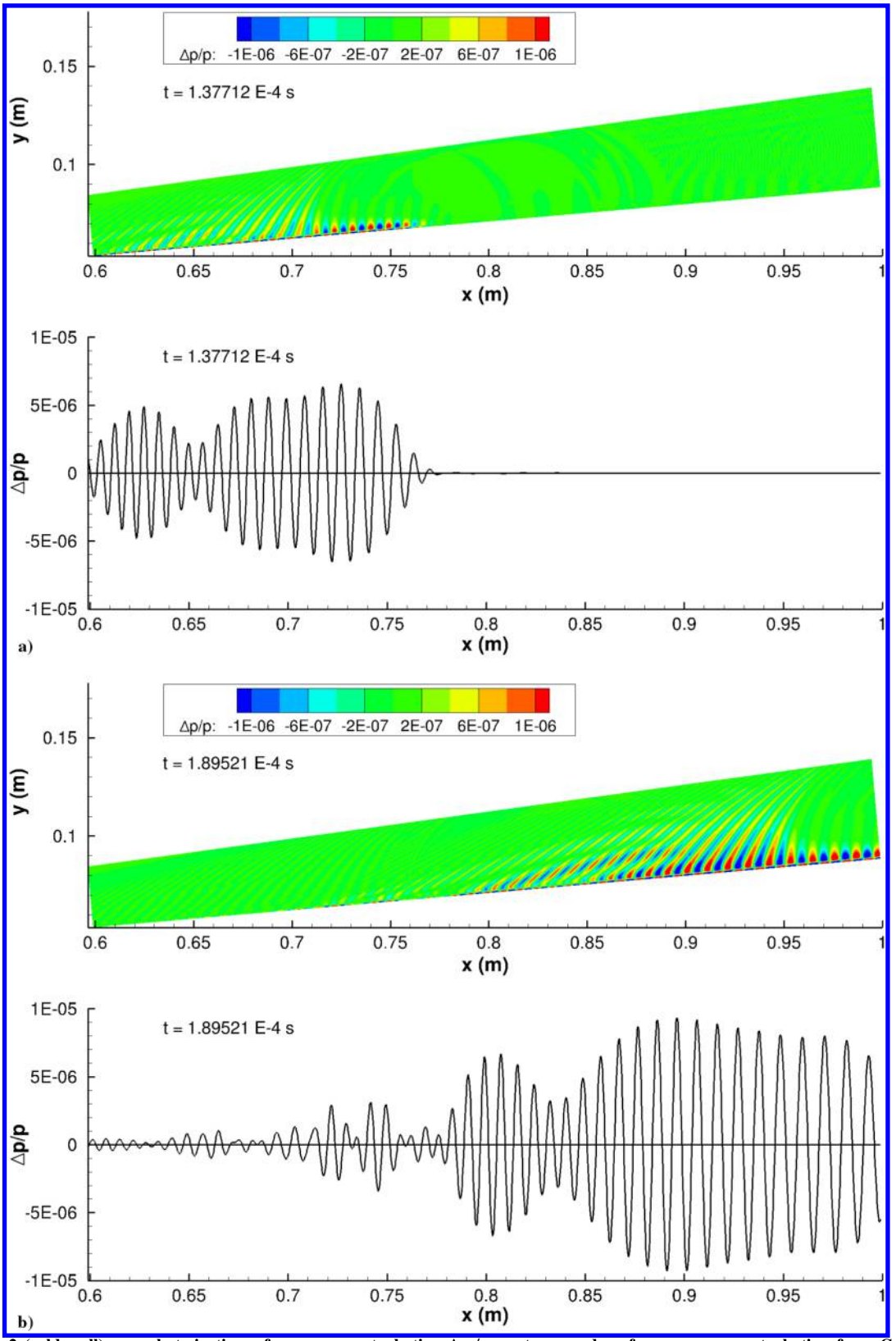

Fig. 17 Case 2 (cold wall), snapshots in time of pressure perturbation $\Delta p/p$ contours and surface pressure perturbation from Gaussian pulse. $\Delta t = 5.181E-5s$.

decrease. This scenario would explain the sound radiation in the freestream and the decay of the perturbation at the wall observed in Fig. 14. This type of modal interaction is indeed very similar to the creation of the supersonic mode; however, it is not predicted by LST because of the assumption that each mode acts independently. In the creation of the supersonic mode, the discrete mode undergoes significant modulation and can be predicted by LST. However, the discrete mode S does not have a supersonic phase speed ($c_r < 1 - 1/M_\infty$), and mode F1 is predicted to be stable by LST. Therefore, because the supersonic mode in this flow is the result of the interaction of modes, it is not expected that the radiation of sound will be apparent with the current LST formulation. It is possible, however, that other nonlinear PSE solvers may resolve the supersonic mode in this flow.

In other flows where mode F1 is predicted to be unstable by LST (see Knisely and Zhong [28]), the supersonic mode can be resolved by LST. However, when mode S is predicted to be unstable by LST, it is possible that a nonlinear interaction of modes can lead to the supersonic mode. When this is the case, the current LST formulation fails to predict the supersonic mode, and other methods, such as DNS or nonlinear PSE, must be used to resolve the supersonic mode. To investigate the relative contribution of each mode to the DNS disturbance, a multimode decomposition using methods and tools developed by Gaydos and Tumin [47] and Miselis et al. [48] must be performed.

B. Case 2 Unsteady Direct Numerical Simulation Results

Similar to case 1, the evolution of the Gaussian pulse in case 2 is visualized in Fig. 17 using snapshots in time of contours of $\Delta p/p$, with the waveform representing the same value at the surface of the cone. The traditional second-mode growth can be seen in Fig. 17a between $x = 0.71$ and $x = 0.77$ m. However, again contrary to the LST predictions, the start of the spontaneous radiation of sound appears in Fig. 17a for $x < 0.71$ m. When the pulse travels farther downstream, the spontaneous radiation of sound becomes much more apparent, shown in Fig. 17b. In particular, the sound radiation is shown very clearly between $x = 0.7$ m and $x = 0.95$ m. The magnitude of the surface pressure perturbation in this region of sound radiation (near $x = 0.89$ m) is actually larger than the traditional second mode ($x > 0.95$ m), which is not observed in case 1. Further Fourier decomposition analysis is performed to compare the DNS perturbation to the LST results.

An FFT was performed on the time history of the surface pressure perturbation at all streamwise locations, resulting in the contour map in Fig. 18a. The neutral stability curve predicted by LST from Fig. 10a is overlaid in Fig. 18a for comparison. The FFT contour generally follows the LST prediction; however, the FFT shows streaky behavior, with certain frequencies being amplified significantly more than their neighboring frequencies. It is possible that this selective frequency amplification is an artifact of the supersonic mode, as suggested by Chuvakhov and Fedorov [25]. Indeed, when visualizing the FFT data versus frequency for fixed streamwise locations (Fig. 18b), there appear multiple peak frequencies for each fixed streamwise location, just as observed by Chuvakhov and Fedorov [25].

The FFT of the entire flowfield was performed and is shown in Fig. 19 for 500 kHz. There is a clear amplification in the freestream for $x > 0.7$ m, whereas there is still some amplification near the wall in this region, as opposed to the disturbance near the wall decaying in case 1. This indicates a longer region of sound radiation in case 2 than case 1. To determine the modal composition of the disturbance, comparisons to LST phase speed, growth rate, and pressure eigenfunctions are made in the absence of a multimode decomposition technique.

The phase speed and growth rate calculated from DNS are compared to the LST predictions for a frequency of $f = 500$ kHz in

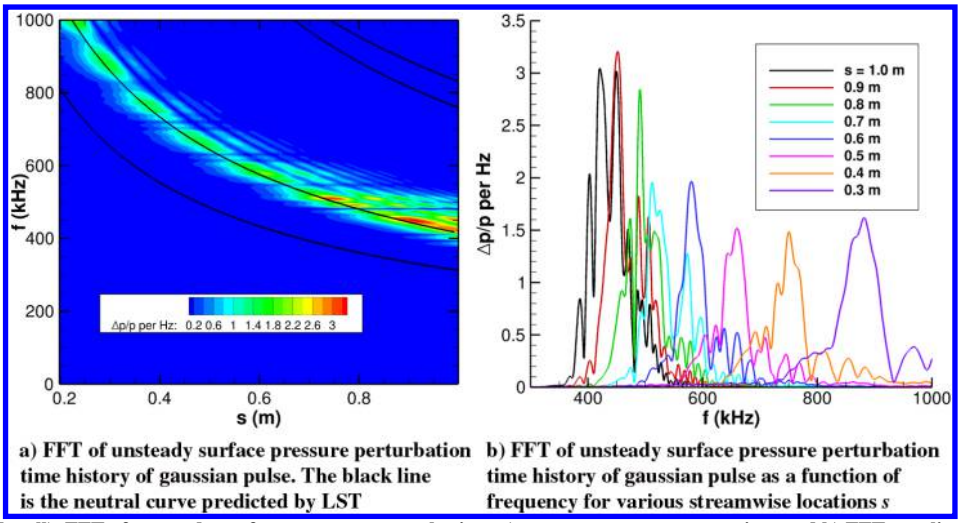

a) FFT of unsteady surface pressure perturbation time history of gaussian pulse. The black line is the neutral curve predicted by LST

b) FFT of unsteady surface pressure perturbation time history of gaussian pulse as a function of frequency for various streamwise locations s

Fig. 18 Case 2 (cold wall), FFT of unsteady surface pressure perturbation: a) contour map representation, and b) FFT amplitude as a function of f.

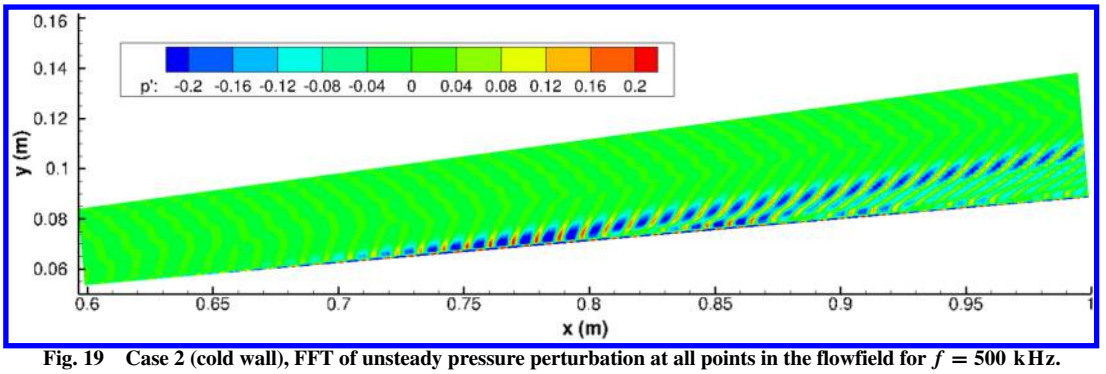

Fig. 19 Case 2 (cold wall), FFT of unsteady pressure perturbation at all points in the flowfield for $f = 500$ kHz.

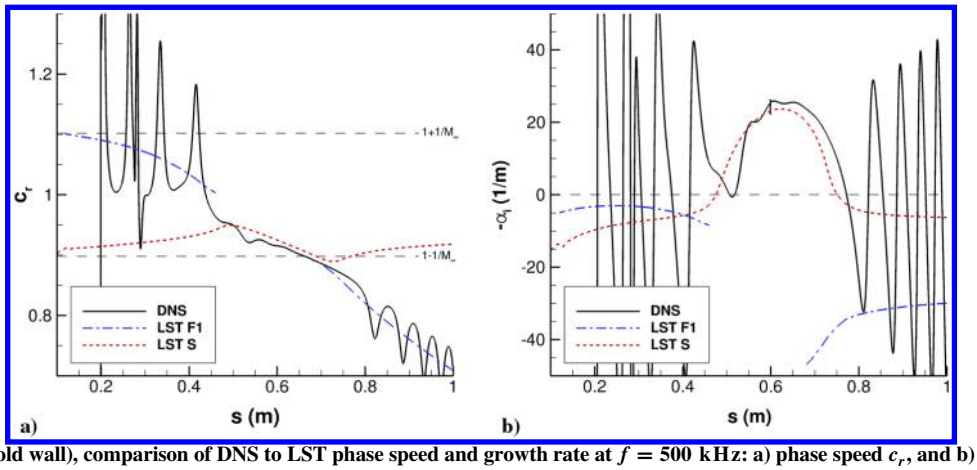

Fig. 20 Case 2 (cold wall), comparison of DNS to LST phase speed and growth rate at $f = 500$ kHz: a) phase speed c_r, and b) growth rate $-\alpha_i$.

Fig. 20. The DNS matches the LST predictions reasonably well for $0.4 < s < 0.75$ m, with significant oscillations in both phase speed and growth rate for $s < 0.4$ m and $s > 0.75$ m. In the region $0.4 < s < 0.75$ m, the DNS growth rate and phase speed are similar to the LST mode S growth rate and phase speed. However, downstream of $s = 0.75$ m, the DNS phase speed continues to follow the supersonic mode F1 phase speed, rather than the dominant mode S. This type of situation is atypical. There are multiple competing modes in DNS; however, there is usually a single dominant mode in this region of instability. In this particular case, the resonant interaction between mode S, mode F1, and the slow acoustic spectrum is strong enough to cause mode F1 to become the dominant instability over mode S. Therefore, the DNS phase speed and growth rate oscillations for $s > 0.75$ m are centered about the supersonic (yet stable according to LST) mode F1. This region of supersonic disturbance propagation causes the sound radiation observed in Figs. 17 and 19.

Comparing the pressure eigenfunctions from DNS to the LST mode F1 and mode S can aid in identifying the dominant mode in the DNS. Eigenfunction comparisons presented in Fig. 21 at $f = 500$ kHz are made at two locations: $s = 0.65$ m, where mode S is predicted to be unstable and subsonic, and $s = 0.8$ m, where mode S and F1 have just synchronized with the slow acoustic spectrum. At $s = 0.65$ m, the DNS and LST mode S eigenfunctions match well (Fig. 21a), indicating that mode S is the dominant mode in this location. Just after synchronization with the slow acoustic spectrum at $s = 0.8$ m, the agreement between DNS and LST is not as strong (Fig. 21b). The DNS eigenfunction appears to be in between the LST mode S and F1 eigenfunctions, indicating that both modes may be represented in the DNS perturbation. However, the DNS eigenfunction appears to more closely follow the LST mode F1 prediction, particularly for $y < 0.002$ m, indicating the significant contribution of the supersonic mode F1 to the DNS perturbation.

Again, similar to case 1, there is a modal energy exchange causing a resonant amplification of the stable mode F1 disturbance, which acts as a source term and causes sound to radiate away from the wall. However, in case 2, the amplification of mode F1 is significantly greater than in case 1, causing this brief supersonic mode to actually have higher magnitude than the traditional second mode. The higher magnitude of the supersonic mode is attributed to the colder wall in case 2. Such a high-magnitude resonant amplification has not yet been observed and requires further in-depth study. Although the conclusion for case 2 in particular is that a resonant trimodal interaction between mode F1, mode S, and the slow acoustic spectrum causes the supersonic mode, it is suggested that this mechanism for the creation of the supersonic mode can apply more generally because it is not limited by LST assumptions.

VIII. Conclusions

The flow conditions considered here induced significant thermochemical nonequilibrium in the flow downstream of the stagnation point for both the hot- and cold-wall cases. For both case 1 (hot wall) and case 2 (cold wall), the LST results indicate that mode S is the unstable mode, and therefore no unstable supersonic mode was expected to exist. However, unsteady DNS results of both cases did indicate the presence of sound radiation away from the wall, despite LST predicting mode F1 to be stable and mode S to be subsonic. Further FFT analysis indicated that this sound radiation was not due to the dominant mode S directly but was actually due to the interaction of mode S and mode F1 with the slow acoustic spectrum, a subtle but important distinction. Because mode S is stable and subsonic when this interaction occurs, most LST solvers will not predict the radiative behavior and could affect boundary-layer transition prediction. However, it is possible that other stability solvers, in particular a nonlinear PSE solver, may resolve the supersonic mode due to modal interactions.

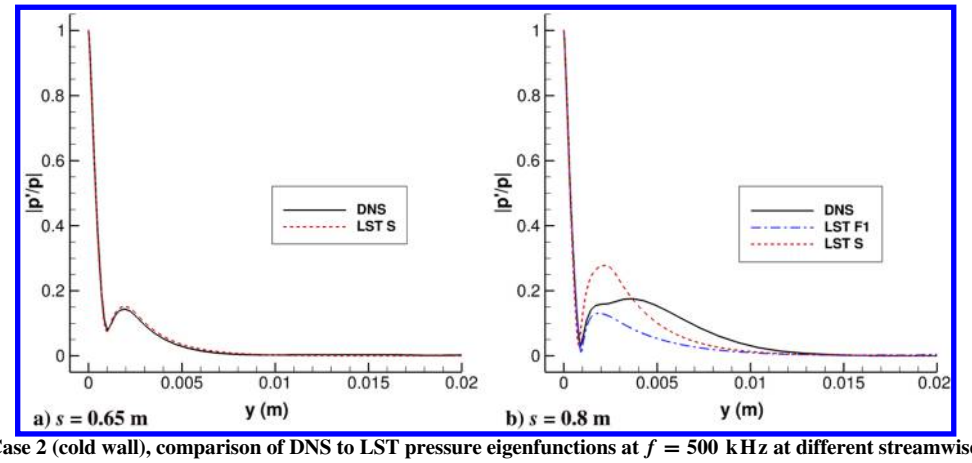

Fig. 21 Case 2 (cold wall), comparison of DNS to LST pressure eigenfunctions at $f = 500$ kHz at different streamwise locations.

Case 2 exhibited a significantly higher-magnitude supersonic mode than case 1, which was attributed to the colder wall. Surprisingly, the supersonic mode in case 2 actually had a higher magnitude than the traditional second mode and could impact transition unexpectedly if not accounted for. Comparison of the DNS phase speed, growth rate, and eigenfunctions justified the explanation that mode F1 became significantly excited while supersonic, resulting in the radiation of sound from the boundary layer. The supersonic mode due to modal interactions demonstrates the need for combined LST and DNS studies such as the one performed here. It is possible that the mechanism creating the supersonic mode may not be thoroughly represented by LST or linear PSE. Further theoretical studies are necessary to assess the shortcomings of LST when studying the supersonic mode. Overall, however, the results are consistent with previous research [24] showing that a colder wall produces a stronger supersonic mode. In both the hot- and cold-wall cases, the radiated sound from the wall may have an impact on the stability of the boundary layer, and it is possible that the sound radiation acts as an energy sink for the second mode [25]. Transition prediction tools such as the e^N method should be used with caution when applied to hypersonic boundary layers with the supersonic mode.

Acknowledgments

This research was supported by the U.S. Air Force Office of Scientific Research (AFOSR) through the National Defense Science and Engineering Graduate Fellowship Program. This research was also partially supported by the AFOSR under grant FA9550-15-1-0268, monitored by Ivett Leyva, and by the Office of Naval Research grant N00014-17-1-2343, monitored by Knox Millsaps previously and by Eric Marineau presently. Primary computational resources were provided by the AFOSR, with additional computational resources provided by Extreme Science and Engineering Discovery Environment through the Texas Advanced Computing Center and San Diego Supercomputer Center under grant TG-ASC090076, supported in part by the National Science Foundation. The views and conclusions contained herein are those of the authors and should not be interpreted as necessarily representing the official policies or endorsements, either expressed or implied, of the U.S. Air Force Office of Scientific Research, Office of Naval Research, or the U.S. Government.

References

[1] Reshotko, E., "Hypersonic Stability and Transition," *Hypersonic Flows for Reentry Problems*, Vol. 1, No. A93-42576 17-02, 1991, pp. 18–34, https://ntrs.nasa.gov/search.jsp?R=19930058582.

[2] Zhong, X., and Wang, X., "Direct Numerical Simulation on the Receptivity, Instability, and Transition of Hypersonic Boundary Layers," *Annual Review of Fluid Mechanics*, Vol. 44, 2012, pp. 527–561. doi:10.1146/annurev-fluid-120710-101208

[3] Fedorov, A., "Transition and Stability of High-Speed Boundary Layers," *Annual Review of Fluid Mechanics*, Vol. 43, 2011, pp. 79–95. doi:10.1146/annurev-fluid-122109-160750

[4] Mack, L. M., "Boundary Layer Linear Stability Theory," AGARD TR 709, Neuilly sur Seine, France, 1984.

[5] Morkovin, M. V., "Transition at Hypersonic Speeds," NASA CR 178315, 1987.

[6] Mack, L. M., "On the Inviscid Acoustic-Mode Instability of Supersonic Shear Flows Part 1: Two-Dimensional Waves," *Theoretical Computational Fluid Dynamics*, Vol. 2, No. 2, 1990, pp. 97–123.

[7] Gushchin, V., and Fedorov, A., "Asymptotic Analysis of Inviscid Perturbations in a Supersonic Boundary Layer," *Journal of Applied Mechanics and Technical Physics*, Vol. 30, No. 1, 1989, pp. 64–70. doi:10.1007/BF00860706

[8] Gushchin, V., and Fedorov, A., "Excitation and Development of Unstable Disturbances in a Supersonic Boundary Layer," *Fluid Dynamics (Izvestiya Akademii Nauk SSSR, Mekhanika Zhidkosti i Gaza)*, Vol. 25, No. 3, 1990, pp. 344–352.

[9] Zhong, X., and Ma, Y., "Boundary-Layer Receptivity of Mach 7.99 Flow over a Blunt Cone to Free-Stream Acoustic Waves," *Journal of Fluid Mechanics*, Vol. 556, June 2006, pp. 55–103. doi:10.1017/S0022112006009293

[10] Parsons, N., Zhong, X., Kim, J., and Eldredge, J., "Numerical Study of Hypersonic Receptivity with Thermochemical Non-Equilibrium on a Blunt Cone," *40th Fluid Dynamics Conference and Exhibit*, AIAA Paper 2010-4446, 2010.

[11] Heitmann, D., and Radespiel, R., "Simulation of the Interaction of a Laser Generated Shock Wave with a Hypersonic Conical Boundary Layer," *41st AIAA Fluid Dynamics Conference and Exhibit*, AIAA Paper 2011-3875, 2011.

[12] Demetriades, A., "Hypersonic Viscous Flow over a Slender Cone; Part III: Laminar Instability and Transition," *7th Fluid and Plasma Dynamics Conference*, AIAA Paper 1974-0535, 1974.

[13] Zhang, C.-H., Tang, Q., and Lee, C.-B., "Hypersonic Boundary-Layer Transition on a Flared Cone," *Acta Mechanica Sinica*, Vol. 29, No. 1, 2013, pp. 48–54. doi:10.1007/s10409-013-0009-2

[14] Fedorov, A., Bres, G., Inkman, M., and Colonius, T., "Instability of Hypersonic Boundary Layer on a Wall with Resonating Micro-Cavities," *49th AIAA Aerospace Sciences Meeting*, AIAA Paper 2011-0373, 2011.

[15] Mack, L., "Review of Linear Compressible Stability Theory," *Stability of Time Dependent and Spatially Varying Flows*, edited by D. Dwoyer, and M. Hussaini, Springer–Verlag, New York, 1985, pp. 164–187.

[16] Chang, C.-L., Vinh, H., and Malik, M., "Hypersonic Boundary-Layer Stability with Chemical Reactions Using PSE," *28th Fluid Dynamics Conference*, AIAA Paper 1997-2012, 1997.

[17] Wagnild, R., "High Enthalpy Effects on Two Boundary Layer Disturbances in Supersonic and Hypersonic Flow," Ph.D. Thesis, Univ. of Minnesota, Minneapolis, MN, 2012.

[18] Bres, G., Inkman, M., Colonius, T., and Fedorov, A., "Second-Mode Attenuation and Cancellation by Porous Coatings in a High-Speed Boundary Layer," *Journal of Fluid Mechanics*, Vol. 726, July 2013, pp. 312–337. doi:10.1017/jfm.2013.206

[19] Klentzman, J., and Tumin, A., "Stability and Receptivity of High Speed Boundary Layers in Oxygen," *43rd Fluid Dynamics Conference*, AIAA Paper 2013-2882, 2013.

[20] Jewell, J., "Boundary-Layer Transition on a Slender Cone in Hypervelocity Flow with Real Gas Effects," Ph.D. Thesis, California Inst. of Technology, Pasadena, CA, 2014.

[21] Fedorov, A., Soudakov, V., and Leyva, I., "Stability Analysis of High-Speed Boundary-Layer Flow with Gas Injection," *7th AIAA Theoretical Fluid Mechanics Conference*, AIAA Paper 2014-2498, 2014.

[22] Salemi, L., "Numerical Investigation of Hypersonic Conical Boundary-Layer Stability Including High-Enthalpy and Three-Dimensional Effects," Ph.D. Thesis, Univ. of Arizona, Tucson, AZ, 2016.

[23] Sescu, A., Sawaya, J., Sassanis, V., and Visbal, M., "Study of the Effect of Two-Dimensional Wall Non-Uniformities on High-speed Boundary Layers," *47th AIAA Fluid Dynamics Conference*, AIAA Paper 2017-4511, 2017.

[24] Bitter, N., and Shepherd, J., "Stability of Highly Cooled Hypervelocity Boundary Layers," *Journal of Fluid Mechanics*, Vol. 778, Sept. 2015, pp. 586–620. doi:10.1017/jfm.2015.358

[25] Chuvakhov, P., and Fedorov, A., "Spontaneous Radiation of Sound by Instability of a Highly Cooled Hypersonic Boundary Layer," *8th AIAA Flow Control Conference*, AIAA Paper 2016-4245, 2016.

[26] Chuvakhov, P., and Fedorov, A., "Spontaneous Radiation of Sound by Instability of a Highly Cooled Hypersonic Boundary Layer," *Journal of Fluid Mechanics*, Vol. 805, Oct. 2016, pp. 188–206. doi:10.1017/jfm.2016.560

[27] Edwards, L., and Tumin, A., "Real Gas Effects on Receptivity to Kinetic Fluctuations: I. Mean Flow Effect," *55th AIAA Aerospace Sciences Meeting*, AIAA Paper 2017-0070, 2017.

[28] Knisely, C., and Zhong, X., "An Investigation of Sound Radiation by Supersonic Unstable Modes in Hypersonic Boundary Layers," *47th AIAA Fluid Dynamics Conference*, AIAA Paper 2017-4516, 2017.

[29] Knisely, C., and Zhong, X., "Supersonic Modes in Hot-Wall Hypersonic Boundary Layers with Thermochemical Nonequilibrium Effects," *2018 AIAA Aerospace Sciences Meeting*, AIAA Paper 2018-2085, 2018.

[30] Knisely, C., and Zhong, X., "The Supersonic Mode and the Role of Wall Temperature in Hypersonic Boundary Layers with Thermochemical Nonequilibrium Effects," *Fluid Dynamics Conference*, AIAA Paper 2018-3218, 2018.

[31] Mortensen, C. H., "Toward an Understanding of Supersonic Modes in Boundary-Layer Transition for Hypersonic Flow over Blunt Cones," *Journal of Fluid Mechanics*, Vol. 846, July 2018, pp. 789–814. doi:10.1017/jfm.2018.246

[32] Mortensen, C. H., and Zhong, X., "High-Order Shock-Fitting Method for Hypersonic Flow with Graphite Ablation and Boundary Layer Stability," *42nd AIAA Fluid Dynamics Conference and Exhibit*, AIAA Paper 2012-3150, 2012.

[33] Mortensen, C. H., and Zhong, X., "Numerical Simulation of Graphite Ablation Induced Outgassing Effects on Hypersonic Boundary Layer Receptivity over a Cone Frustum," *51st AIAA Aerospace Sciences Meeting*, AIAA Paper 2013-0522, 2013.

[34] Mortensen, C. H., and Zhong, X., "Real Gas and Surface Ablation Effects on Hypersonic Boundary Layer Instability over a Blunt Cone," *43rd Fluid Dynamics Conference*, AIAA Paper 2013-2981, 2013.

[35] Mortensen, C. H., and Zhong, X., "Simulation of Second-Mode Instability in a Real-Gas Hypersonic Flow with Graphite Ablation," *AIAA Journal*, Vol. 52, No. 8, 2014, pp. 1632–1652. doi:10.2514/1.J052659

[36] Mortensen, C. H., and Zhong, X., "Numerical Simulation of Hypersonic Boundary-Layer Instability in a Real Gas with Two-Dimensional Surface Roughness," *45th AIAA Fluid Dynamics Conference*, AIAA Paper 2015-3077, 2015.

[37] Mortensen, C. H., "Effects of Thermochemical Nonequilibrium on Hypersonic Boundary-Layer Instability in the Presence of Surface Ablation and Isolated Two-Dimensional Roughness," Ph.D. Thesis, Univ. of California, Los Angeles, Los Angeles, 2015.

[38] Prakash, A., Parsons, N., Wang, X., and Zhong, X., "High-Order Shock-Fitting Methods for Direct Numerical Simulation of Hypersonic Flow with Chemical and Thermal Nonequilibrium," *Journal of Computational Physics*, Vol. 230, No. 23, 2011, pp. 8474–8507. doi:10.1016/j.jcp.2011.08.001

[39] Williamson, J., "Low-Storage Runge–Kutta Schemes," *Journal of Computational Physics*, Vol. 35, No. 1, 1980, pp. 48–56. doi:10.1016/0021-9991(80)90033-9

[40] Malik, M. R., "Numerical Methods for Hypersonic Boundary Layer Stability," *Journal of Computational Physics*, Vol. 86, No. 2, 1990, pp. 376–413. doi:10.1016/0021-9991(90)90106-B

[41] Anderson, E., Bai, Z., Bischof, C., Blackford, S., Demmel, J., Garra, J. D., Croz, J. D., Greenbaum, A., Hammarling, S., McKenney, A., et al., *LAPACK Users' Guide*, 3rd ed., Soc. for Industrial and Applied Mathematics, Philadelphia, 1999, Chap. 2.3.

[42] Malik, M. R., "Hypersonic Flight Transition Data Analysis Using Parabolized Stability Equations with Chemistry Effects," *Journal of Spacecraft and Rockets*, Vol. 40, No. 3, 2003, pp. 332–344. doi:10.2514/2.3968

[43] Fedorov, A., and Tumin, A., "High-Speed Boundary-Layer Instability: Old Terminology and a New Framework," *AIAA Journal*, Vol. 49, No. 8, 2011, pp. 1647–1657. doi:10.2514/1.J050835

[44] Ma, Y., and Zhong, X., "Receptivity of a Supersonic Boundary Layer over a Flat Plate. Part 1. Wave Structures and Interactions," *Journal of Fluid Mechanics*, Vol. 488, July 2003, pp. 31–78. doi:10.1017/S0022112003004786

[45] Ma, Y., and Zhong, X., "Receptivity of a Supersonic Boundary Layer over a Flat Plate. Part 2. Receptivity to Free-Stream Sound," *Journal of Fluid Mechanics*, Vol. 488, July 2003, pp. 79–121. doi:10.1017/S0022112003004798

[46] Ma, Y., and Zhong, X., "Receptivity of a Supersonic Boundary Layer over a Flat Plate. Part 3. Effects of Different Types of Free-Stream Disturbances," *Journal of Fluid Mechanics*, Vol. 532, June 2005, pp. 63–109. doi:10.1017/S0022112005003836

[47] Gaydos, P., and Tumin, A., "Multimode Decomposition in Compressible Boundary Layers," *AIAA Journal*, Vol. 42, No. 6, 2004, pp. 1115–1121. doi:10.2514/1.2289

[48] Miselis, M., Huang, Y., and Zhong, X., "Modal Analysis of Receptivity Mechanisms for a Freestream Hot-Spot Perturbation on a Blunt Compression-Cone Boundary Layer," *46th AIAA Fluid Dynamics Conference*, AIAA Paper 2016-3345, 2016.

J. Poggie
Associate Editor